

# Empirical Evaluation of PRNU Fingerprint Variation for Mismatched Imaging Pipelines

Sharad Joshi<sup>1</sup>, Pawel Korus<sup>2,3</sup>, Nitin Khanna<sup>1</sup>, and Nasir Memon<sup>2</sup>

<sup>1</sup>MANAS Lab, Indian Institute of Technology Gandhinagar, India

<sup>2</sup>Tandon School of Engineering, New York University, USA

<sup>3</sup>Department of Telecommunications, AGH University of Science and Technology, Poland

e-mail: {sharad.joshi,nitinkhanna}@iitgn.ac.in, {pkorus,memon}@nyu.edu

**Abstract**—We assess the variability of PRNU-based camera fingerprints with mismatched imaging pipelines (e.g., different camera ISP or digital darkroom software). We show that camera fingerprints exhibit non-negligible variations in this setup, which may lead to unexpected degradation of detection statistics in real-world use-cases. We tested 13 different pipelines, including standard digital darkroom software and recent neural-networks. We observed that correlation between fingerprints from mismatched pipelines drops on average to 0.38 and the PCE detection statistic drops by over 40%. The degradation in error rates is the strongest for small patches commonly used in photo manipulation detection, and when neural networks are used for photo development. At a fixed 0.5% FPR setting, the TPR drops by 17 ppt (percentage points) for 128 px and 256 px patches.

## I. INTRODUCTION

Camera fingerprints based on photo-response non-uniformity (PRNU) of the imaging sensor are one of the most reliable tools in photo forensics [1–3]. They have been studied in the literature for over a decade [4–7] and are commonly used in two main applications: (1) *source attribution* - which links photographs to a specific instance of a camera; and (2) *photo manipulation detection* - which involves a local analysis of the sensor fingerprint to identify areas of mismatch [8].

The success of PRNU fingerprints stems from their stability and robustness to various post-processing that happens in real-world applications (e.g., scaling, or lossy compression). Some of this post-processing, in particular the impact of JPEG compression or denoising, have been extensively studied [9–12]. However, many others remain unexplored. This may lead to inaccurate detection and under-estimated error rates.

In this work, we empirically assess the sensitivity of PRNU fingerprints to *mismatched imaging pipelines*. This scenario arises when test images are processed differently (e.g., using 3rd-party darkroom software like LibRAW or Lightroom) than the images used for fingerprint estimation. We believe this scenario will become increasingly more common with the progress of machine learning and the increasing adoption of deep neural networks in various stages of the imaging pipeline (e.g., demosaicing [13], denoising [14], or tone-mapping [15]) or even instead of it [16]. Moreover, modern darkrooms, e.g., *Luminar*, extensively advertise ML-based solutions in their image processing and enhancement routines, and such a trend is likely to increase.

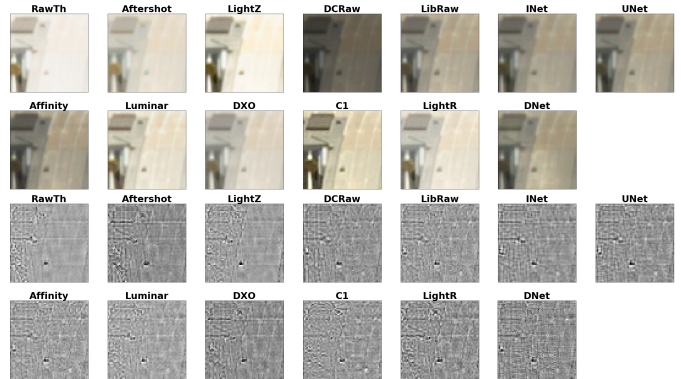


Fig. 1. Image patches of size  $64 \times 64$  px (top) and their residuals (bottom) from 13 different imaging pipelines operating with default settings.

In this work, we take the first step in this direction and assess the impact of image signal processor (ISP) i.e., imaging pipeline variation on PRNU fingerprint analysis. We used 13 software pipelines representing popular digital darkrooms and 3 neural network architectures. We consider a scenario where each pipeline uses default settings with minimal post-processing, and neural-network is trained to reproduce images visually equivalent to a standard camera pipeline [17, 18] (see Figure 1 for example image patches and residuals for Nikon D7000).

The main observations from our work are as follows:

- Correlation between camera fingerprints obtained from exactly the same images processed by different pipelines drops on average by 62 %.
- Degradation in detection statistics is the strongest for smaller image patches (128 or 256 px windows), which will be particularly detrimental to manipulation detection.
- For large patches (1024 px), standard ISPs reveal little variation in detection statistics, but the effect remains strong for neural ISPs.
- For 128 px windows commonly used in manipulation detection, we observed an average deterioration of 41% in median PCE and of 17% in TPR at 0.5% FPR.
- Imaging pipelines based on neural networks tend to distort the camera fingerprints more - TPR dropped by 20% compared to 14% for standard pipelines.

- Even for traditional pipelines, we observed unexpected matching failures for some configurations (*RawTherapee* and *Capture One* software with Nikon cameras).

## II. BACKGROUND AND RELATED WORK

A PRNU fingerprint of a camera characterizes the consistent bias of individual pixels in its imaging sensor [8]. The fingerprint is estimated from multiple images by carefully averaging high-frequency residuals where a denoising filter suppresses content. At first, a noise residual  $R_i$  is computed for each input image  $I_i$  using a denoising filter  $D$  as  $R_i = I_i - D(I_i)$ ,  $i = 1, \dots, N$ . In the next step, the fingerprint  $k$  is estimated using maximum likelihood estimation [8]:

$$k = \frac{\sum_{i=1}^N R_i I_i}{\sum_{i=1}^N (I_i)^2} \quad (1)$$

At test time, the corresponding residual of a test image is correlated with the camera fingerprint - either globally (for attribution) or locally (for manipulation detection).

Several enhancement techniques have been proposed to reduce contamination of PRNU by the image content. Kang *et al.* [19] proposed a method that estimates PRNU only from the phase components of noise residuals. Lin and Li [20] proposed smoothing the Fourier spectrum of the estimated PRNU using local averaging. These two methods were based on the hypothesis that the sensor pattern noise is white noise (i.e., it has a flat frequency spectrum). On the other hand, Li [21] assume that PRNU is a weak signal, while scene details are likely to be much stronger. They proposed several models that produce weighted versions of wavelet coefficients of a noise residual. An inverse wavelet transform on the weighted coefficients provides the enhanced noise residuals.

Various denoising filters have also been evaluated in the literature. These include a context-adaptive interpolator (CAI) [5], 2-pixel approach [22], adaptive spatial (AS) filtering [23], content adaptive guided image (CAGI) filtering [24], and block-matching and 3D (BM3D) algorithm [12, 25]. A recent method proposed usage of a convolutional neural network (CNN) to improve the estimation of noise residual extracted by traditional means [26].

The large size and random nature of sensor fingerprints combined with a computationally expensive fingerprint matching create difficulty in managing large databases. Many methods have proposed alternative representations [27–30] of the PRNU fingerprint. A recent method attempts to use a fused CNN-based approach that combines camera model features and PRNU to improve small-scale tampering detection [31].

Despite addressing a sensor-level phenomenon, the analysis is typically performed in the RGB color space. As a result, the fingerprint is affected by various steps in the camera’s ISP, e.g., demosaicing, denoising, or tone-mapping. Some researchers have proposed exploiting knowledge of specific camera components to estimate a better fingerprint, e.g., given the color filter array, one can consider only the measured

color channels [32]. Alternatively, a more recent line of work explores inversion of the ISP and estimation at the raw level [33, 34].

## III. EXPERIMENTAL RESULTS AND DISCUSSION

To assess the impact of the image processing pipeline (ISP) on PRNU fingerprints, we construct a new dataset derived from *raw* images from 4 cameras and 13 different ISPs. We then follow the standard fingerprint estimation procedure [8] and assess the impact on: (1) the correlation between different fingerprint estimates; (2) the distributions of PCE scores obtained with mismatched estimation and test ISPs; (3) the receiver operation statistics and relevant detection metrics (AUC and TPR at FPR=0.5%).

### A. Dataset and Fingerprint Estimation

We collected *raw* images for 4 cameras: Nikon D7000 (N7k), Nikon D90 (N90), Canon EOS 40D (C4D) and Canon EOS 5D (C5D). The Nikon and Canon images were taken from the Raise [35], and MIT-5k [36] datasets, respectively (Table I). We collected 120 full-resolution images, out of which 60 were used for PRNU estimation and 60 for subsequent attribution experiments.

We then processed all images using 13 different ISPs. We included popular digital darkroom software (both commercial and open-source) as well as recent neural-network-based ISPs. We included 10 darkrooms: RawTherapee 5.6 (RT) [37], Corel AfterShot Pro 3 (AT) [38] LightZone 4.1.9 (LZ) [39], DCRaw 9.27 (DR) [40], LibRaw 0.17.2 (LR) [41], Affinity Photo 1.6.6 (AF) [42], Luminar 3 (LR) [43], DXO PhotoLab 2 (DX) [44], Capture One 12 (C1) [45], and Adobe Lightroom 5 (LT) [46]. The neural ISPs included a popular model for joint demosaicing and denoising (DNet) [47], the UNet (UN) [48] model, and a simple network that mimics a standard ISP (INet) [17]. All NN models were trained to reproduce the result of a standard imaging pipeline.

To assess the most optimistic scenario, we made sure to: (1) select the same images for PRNU estimation; (2) use an *automatic* mode with default settings and no scaling in each ISP; (3) work on uncompressed bitmap images. In a real-world setting, these conditions are unlikely to be met.

### B. Analysis of Camera Fingerprint Similarity

To compare the PRNU fingerprints, we compute the normalized correlation coefficients between all possible pairs of estimation pipelines. If necessary, we align the fingerprints by shifting one of them to the location indicated by a peak in cross-correlation (needed sometimes due to minor differences in how ISPs crop the *raw* images; see Table V in the supplemental file).

We collected the obtained results in Table II for all four cameras. It can be observed that despite a conservative evaluation setting, the estimated fingerprints tend to differ considerably. The average correlation for all cross-ISP pairs is only 0.38. Some of the ISPs, e.g., DCRaw, LibRaw, and Affinity, tend to correlate better, which may indicate some

TABLE I  
DIMENSIONS OF PROCESSED IMAGES OBTAINED USING ALL PIPELINES IN OUR DATASET

Camera	Camera Processing Pipelines													
	RT	AT	LZ	DR	LR	AF	LM	DX	C1	LT	IN	UN	DN	
N7k	3272 x 4940	3264 x 4928	3270 x 4938	3280 x 4948	3280 x 4948	3280 x 4948	3264 x 4928	3264 x 4928	Diff. sizes	3264 x 4928	3280 x 4948	3280 x 4948	3280 x 4948	
N90	2860 x 4302	2860 x 4290	2858 x 4300	2868 x 4310	2868 x 4310	2868 x 4310	2848 x 4288	2848 x 4288	Diff. sizes	2848 x 4288	2868 x 4310	2868 x 4310	2868 x 4310	
C4D	2594 x 3900	-	2592 x 3898	2602 x 3908	2602 x 3908	2602 x 3908	2592 x 3888	2592 x 3888	2592 x 3888	2592 x 3888	2602 x 3908	2602 x 3908	2602 x 3908	
C5D	2912 x 4378	-	2910 x 4376	2920 x 4386	2920 x 4386	2920 x 4386	2912 x 4368	2912 x 4368	2912 x 4368	Diff. sizes	2920 x 4386	2920 x 4386	2920 x 4386	

TABLE II  
CORRELATION COEFFICIENTS BETWEEN PRNU FINGERPRINTS USING DIFFERENT IMAGING PIPELINES.

	RT	AT	LZ	DR	LR	AF	LM	DX	C1	LT	IN	UN	DN
Nikon D7000													
RT	<b>1.00</b>	<b>0.03</b>	<b>0.02</b>	<b>0.02</b>	<b>0.02</b>	<b>0.02</b>	<b>0.02</b>	<b>0.03</b>	<b>0.00</b>	<b>0.03</b>	<b>0.02</b>	<b>0.02</b>	<b>0.02</b>
AT	<b>0.03</b>	<b>1.00</b>	0.45	0.40	0.42	0.43	0.35	0.78	<b>0.01</b>	0.69	0.34	0.33	0.56
LZ	<b>0.02</b>	0.45	<b>1.00</b>	0.65	0.71	0.71	0.45	0.50	<b>0.00</b>	0.50	0.24	0.58	0.42
DR	<b>0.02</b>	0.40	0.65	<b>1.00</b>	0.89	0.88	0.44	0.46	<b>0.00</b>	0.46	0.26	0.65	0.45
LR	<b>0.02</b>	0.42	0.71	0.89	<b>1.00</b>	0.93	0.50	0.48	<b>0.00</b>	0.50	0.27	0.69	0.47
AF	<b>0.02</b>	0.43	0.71	0.88	0.93	<b>1.00</b>	0.50	0.49	<b>0.00</b>	0.51	0.28	0.67	0.48
LM	<b>0.02</b>	0.35	0.45	0.44	0.50	0.50	<b>1.00</b>	0.44	<b>0.00</b>	0.51	0.28	0.44	0.44
DX	<b>0.03</b>	0.78	0.50	0.46	0.48	0.49	0.44	<b>1.00</b>	<b>0.01</b>	0.84	0.37	0.39	0.64
C1	<b>0.00</b>	<b>0.01</b>	<b>0.00</b>	<b>0.00</b>	<b>0.00</b>	<b>0.00</b>	<b>0.00</b>	<b>0.01</b>	<b>1.00</b>	<b>0.01</b>	<b>0.01</b>	<b>0.00</b>	<b>0.01</b>
LT	<b>0.03</b>	0.69	0.50	0.46	0.50	0.51	0.51	0.84	<b>0.01</b>	<b>1.00</b>	0.37	0.40	0.65
IN	<b>0.02</b>	0.34	0.24	0.26	0.27	0.28	0.28	0.37	<b>0.01</b>	0.37	<b>1.00</b>	0.28	0.47
UN	<b>0.02</b>	0.33	0.58	0.65	0.69	0.67	0.44	0.39	<b>0.00</b>	0.40	0.28	<b>1.00</b>	0.41
DN	<b>0.02</b>	0.56	0.42	0.45	0.47	0.48	0.44	0.64	<b>0.01</b>	0.65	0.47	0.41	<b>1.00</b>
Nikon D90													
RT	<b>1.00</b>	<b>0.01</b>	<b>0.00</b>	<b>0.01</b>	<b>0.01</b>	<b>0.01</b>	<b>0.01</b>						
AT	<b>0.01</b>	<b>1.00</b>	0.32	0.28	0.30	0.29	0.28	0.39	<b>0.00</b>	0.35	0.15	0.26	0.23
LZ	<b>0.01</b>	0.32	<b>1.00</b>	0.75	0.77	0.79	0.39	0.41	<b>0.01</b>	0.43	0.15	0.62	0.29
DR	<b>0.01</b>	0.28	0.75	<b>1.00</b>	0.83	0.88	0.33	0.35	<b>0.00</b>	0.36	0.14	0.58	0.28
LR	<b>0.01</b>	0.30	0.77	0.83	<b>1.00</b>	0.89	0.39	0.40	<b>0.01</b>	0.42	0.14	0.64	0.31
AF	<b>0.01</b>	0.29	0.79	0.88	0.89	<b>1.00</b>	0.37	0.37	<b>0.01</b>	0.4	0.13	0.6	0.29
LM	<b>0.01</b>	0.28	0.39	0.33	0.39	0.37	<b>1.00</b>	0.7	<b>0.01</b>	0.44	0.11	0.31	0.27
DX	<b>0.01</b>	0.39	0.41	0.35	0.40	0.37	0.70	<b>1.00</b>	<b>0.01</b>	0.47	0.17	0.33	0.30
C1	<b>0.00</b>	<b>0.00</b>	<b>0.01</b>	<b>0.00</b>	<b>0.01</b>	<b>0.01</b>	<b>0.01</b>	<b>0.01</b>	<b>1.00</b>	<b>0.01</b>	<b>0.01</b>	<b>0.00</b>	<b>0.01</b>
LT	<b>0.01</b>	0.35	0.43	0.36	0.42	0.40	0.44	0.47	<b>0.01</b>	<b>1.00</b>	0.25	0.33	0.48
IN	<b>0.01</b>	0.15	0.15	0.14	0.14	0.13	0.11	0.17	<b>0.01</b>	0.25	<b>1.00</b>	0.17	0.38
UN	<b>0.01</b>	0.26	0.62	0.58	0.64	0.60	0.31	0.33	<b>0.00</b>	0.33	0.17	<b>1.00</b>	0.31
DN	<b>0.01</b>	0.23	0.29	0.28	0.31	0.29	0.27	0.30	<b>0.01</b>	0.48	0.38	0.31	<b>1.00</b>
Canon EOS 40D													
RT	<b>1.00</b>	-	0.69	0.74	0.74	0.75	0.70	0.72	0.51	0.71	0.24	0.16	0.59
AT	-	-	-	-	-	-	-	-	-	-	-	-	-
LZ	0.69	-	<b>1.00</b>	0.65	0.72	0.71	0.68	0.82	0.54	0.82	0.24	0.14	0.57
DR	0.74	-	0.65	<b>1.00</b>	0.84	0.84	0.63	0.67	0.45	0.64	0.23	0.17	0.60
LR	0.74	-	0.72	0.84	<b>1.00</b>	0.89	0.71	0.74	0.53	0.72	0.25	0.16	0.66
AF	0.75	-	0.71	0.84	0.89	<b>1.00</b>	0.75	0.71	0.52	0.69	0.24	0.15	0.63
LM	0.70	-	0.68	0.63	0.71	0.75	<b>1.00</b>	0.67	0.57	0.71	0.21	0.12	0.58
DX	0.72	-	0.82	0.67	0.74	0.71	0.67	<b>1.00</b>	0.55	0.84	0.28	0.15	0.60
C1	0.51	-	0.54	0.45	0.53	0.52	0.57	0.55	<b>1.00</b>	0.55	0.17	0.10	0.42
LT	0.71	-	0.82	0.64	0.72	0.69	0.71	0.84	0.55	<b>1.00</b>	0.25	0.15	0.57
IN	0.24	-	0.24	0.23	0.25	0.24	0.21	0.28	0.17	0.25	<b>1.00</b>	0.21	0.26
UN	0.16	-	0.14	0.17	0.16	0.15	0.12	0.15	0.10	0.15	0.21	<b>1.00</b>	0.17
DN	0.59	-	0.57	0.60	0.66	0.63	0.58	0.60	0.42	0.57	0.26	0.17	<b>1.00</b>
Canon EOS 5D													
RT	<b>1.00</b>	-	0.39	0.39	0.40	0.40	0.61	0.32	0.46	0.60	0.28	0.29	0.59
AT	-	-	-	-	-	-	-	-	-	-	-	-	-
LZ	0.39	-	<b>1.00</b>	0.68	0.73	0.74	0.30	0.64	0.24	0.33	0.15	0.55	0.32
DR	0.39	-	0.68	<b>1.00</b>	0.81	0.87	0.28	0.55	0.21	0.28	0.14	0.54	0.32
LR	0.40	-	0.73	0.81	<b>1.00</b>	0.88	0.31	0.61	0.24	0.33	0.15	0.59	0.35
AF	0.40	-	0.74	0.87	0.88	<b>1.00</b>	0.31	0.59	0.24	0.31	0.14	0.57	0.34
LM	0.61	-	0.30	0.28	0.31	0.31	<b>1.00</b>	0.36	0.58	0.72	0.15	0.24	0.51
DX	0.32	-	0.64	0.55	0.61	0.59	0.36	<b>1.00</b>	0.30	0.43	0.12	0.40	0.27
C1	0.46	-	0.24	0.21	0.24	0.24	0.58	0.30	<b>1.00</b>	0.56	0.13	0.17	0.34
LT	0.60	-	0.33	0.28	0.33	0.31	0.72	0.43	0.56	<b>1.00</b>	0.20	0.22	0.46
IN	0.28	-	0.15	0.14	0.15	0.14	0.15	0.12	0.13	0.20	<b>1.00</b>	0.12	0.25
UN	0.29	-	0.55	0.54	0.59	0.57	0.24	0.4	0.17	0.22	0.12	<b>1.00</b>	0.30
DN	0.59	-	0.32	0.32	0.35	0.34	0.51	0.27	0.34	0.46	0.25	0.30	<b>1.00</b>

common components in their functionality (e.g., use of the DCRaw routines in LibRaw [49]).

Interestingly, fingerprints from *CaptureOne* and *RawTherapee* do not correlate with any other ISPs for neither of Nikon cameras (marked in red). Based on visual comparison of image patches, it would appear both programs apply some slight geometric transformation while cropping full-frame *raw* images, which de-synchronizes the fingerprints. We emphasize that this happens despite explicit instructions to leave image size intact and that the problem does not occur for Canon cameras (this may be related to the format of *raw* images in

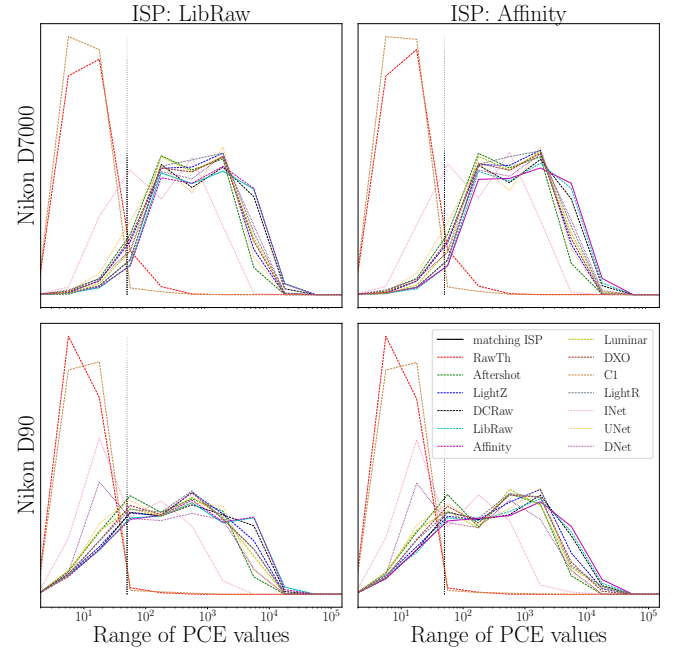


Fig. 2. Distribution of PCE scores for cross-ISP matching (512 px patches); the dashed vertical line shows a common acceptance threshold of 50.

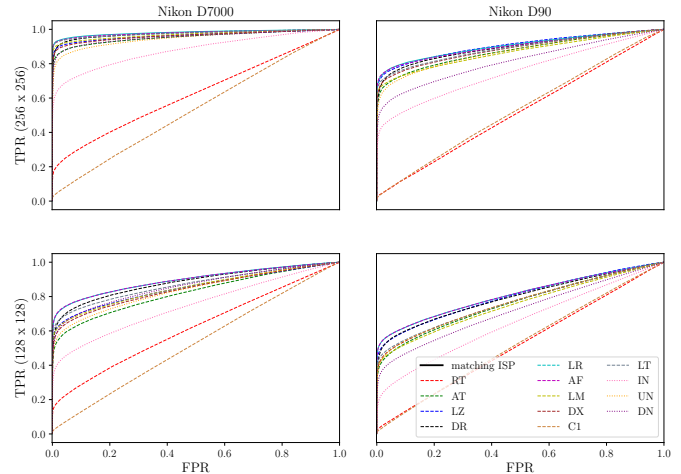


Fig. 3. Receiver operating characteristic (ROC) curves with LibRaw as PRNU estimation ISP and all pipelines as test.

our dataset - NEF for Nikon and DNG for Canon cameras).

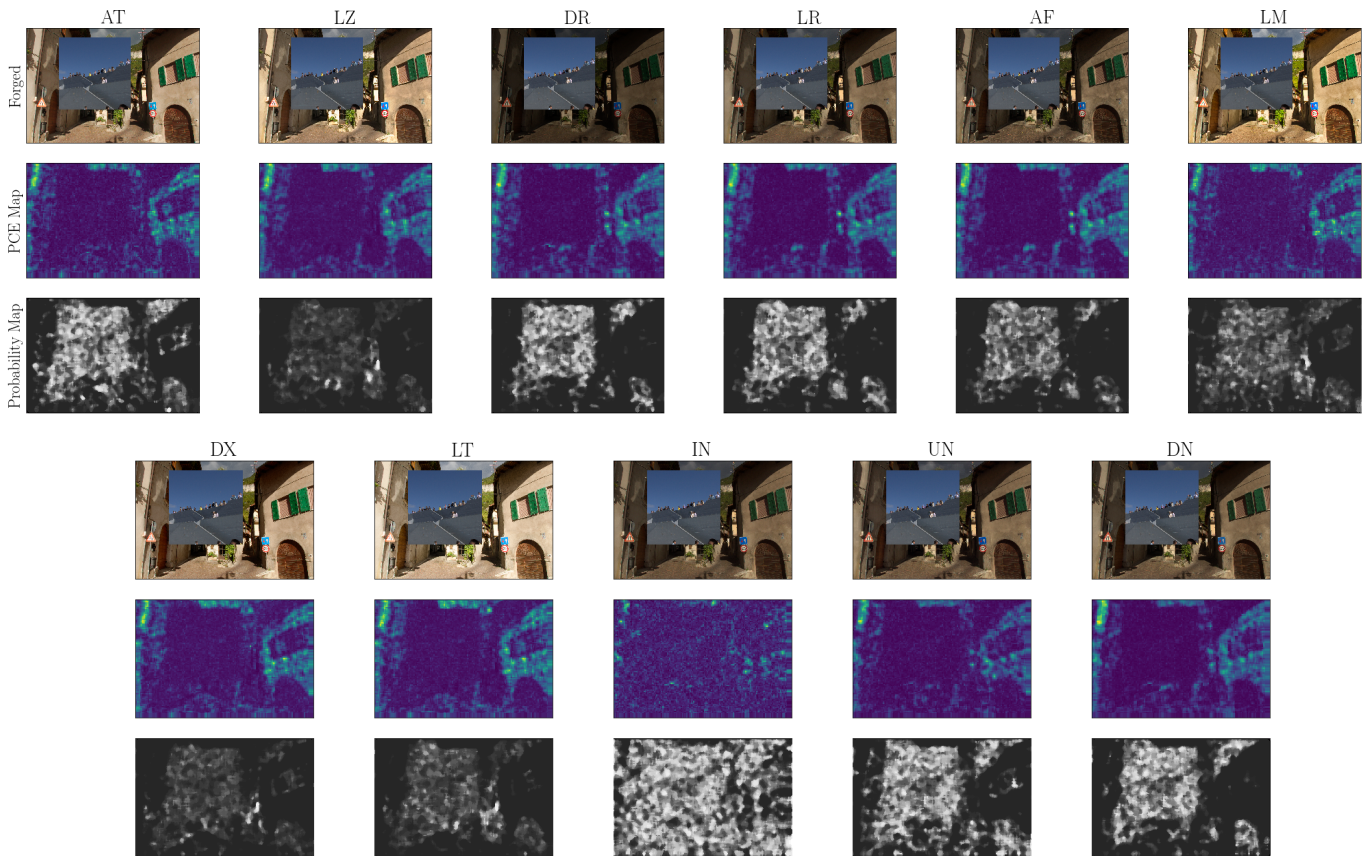


Fig. 4. Example tampering localization results obtained with a camera fingerprint from a mismatched ISP (LibRAW); tampering probability maps were obtained as  $p$ -values from PCE statistics and were post-processed for presentation clarity (contrast + median filter).

### C. Impact on PCE Detection Statistics

To assess the impact on fingerprint detection statistics, we measured peak-to-correlation-energy (PCE) for all possible pairs of ISPs (using different pipelines for PRNU estimation and test images). To increase the number of samples, we extract all possible non-overlapping patches from full-resolution images. This yields from 600 to 55,000 patches for patch sizes ranging from 1024 px to 128 px.

In general, using the same imaging pipeline leads to the best matching performance (see median PCE scores for Nikon D7000 in Table III and Canon EOS 40 D in Table V of the supplemental file). In cross-ISP matching, the PCE deteriorates on average by 61, 56, 50, and 41% for patches of 1024, 512, 256, and 128 px, respectively. Full distributions of PCE scores for 512 px patches from selected cameras and ISPs are shown in Figure 2 (results for all cameras are depicted in Figure 5 of the supplemental file). Note that the PCE distributions are shown in logarithmic scale. Configurations with the same ISP are shown with solid lines, whereas mismatched digital darkrooms and neural ISPs are shown with dashed and dotted lines, respectively.

Overall, we see a similar trend as in fingerprint correlation (Section III-B). Apart from obvious matching failures for *CaptureOne* and *RawTherapee* for Nikon cameras, we observe

various degrees of PCE deterioration. The most significant and consistent deterioration occurs for neural ISPs. In some cases, e.g., for Canon cameras in our experiments, they seemed to have incompatible fingerprints.

### D. Impact on ROC Curves and Error Rates

To assess the impact of ISP mismatch on effective error rates, we generate full receiver operating characteristics (ROC curves). An example set of ROC curves for smaller patch sizes (i.e., 256 and 128 px), selective cameras, and a single PRNU estimation ISP (LibRaw) is shown in Figure 3. Analogously to previous experiments, we can see a significant variation of matching performance with the strongest deterioration for small patch sizes and for neural ISPs.

To quantitatively summarize the degradation, we show true positive rates corresponding to a fixed 0.5% false-positive rate (Table IV). We focus on 128 and 256 px patches due to the much larger number of available samples. For the illustrated LibRaw and Affinity Photo ISPs, the average deterioration in TPR was 17 percentage points (13 ppt for well-synchronized standard darkroom software and 20 ppt for neural ISPs).

## IV. CONCLUSION AND FUTURE WORK

Our results illustrate that camera fingerprints exhibit non-negligible variation with the imaging pipeline. Despite choos-

TABLE III  
MEDIAN PCE VALUES FOR CROSS-PIPELINE ATTRIBUTION OF  
NON-OVERLAPPING PATCHES FROM NIKON D7000

PRNU ISP	Image Processing Pipelines for Test Images												
	RT	AT	LZ	DR	LR	AF	LM	DX	CI	LT	IN	UN	DN
Patch size = 1024 x 1024 pixels (~600 patches per camera per pipeline)													
RT	198	10	10	11	11	11	10	10	10	11	12	13	
AT	10	880	865	978	1105	1176	833	936	10	1072	209	550	926
LZ	11	1617	2324	2338	2714	3087	2333	2071	10	2584	632	1523	2326
DR	11	1591	2042	2840	3169	3389	2355	1982	10	2539	675	1838	2663
LR	11	1766	2310	3060	3538	3802	2647	2242	10	2786	769	2049	3036
AF	10	1672	2137	2770	3300	3626	2520	2113	10	2719	743	1843	2721
LM	12	1915	2692	3635	4252	4355	5098	2977	10	3833	1255	2923	3741
DX	10	926	1046	1187	1385	1471	1233	1170	10	1436	224	699	1183
CI	9	10	9	11	10	10	10	9	15425	10	10	10	12
LT	10	1036	1193	1423	1624	1726	1555	1332	10	3261	306	870	1430
IN	10	206	241	298	343	390	372	217	10	327	733	286	349
UN	11	973	1317	1859	2116	2299	1997	1343	10	1766	704	1927	2010
DN	10	811	973	1218	1399	1513	1171	1018	10	1265	347	821	1444
Patch size = 512 x 512 pixels (~3000 patches per camera per pipeline)													
RT	44	10	10	11	11	11	10	10	10	11	11	11	12
AT	10	200	203	196	221	226	169	218	10	243	44	111	176
LZ	11	427	554	538	626	650	517	519	10	590	135	334	500
DR	11	379	458	653	704	747	479	446	10	525	143	386	557
LR	11	421	527	699	811	856	556	518	10	609	169	437	639
AF	11	437	546	735	846	906	590	541	10	637	187	471	661
LM	11	480	682	757	872	930	1201	718	10	920	245	601	735
DX	10	215	247	239	275	286	250	272	10	327	47	142	224
CI	10	10	10	11	10	10	10	9	3374	10	10	11	11
LT	10	243	288	289	332	346	326	313	10	681	67	182	272
IN	10	45	57	63	69	74	71	46	10	68	142	58	65
UN	11	242	309	429	478	510	421	299	10	373	158	454	447
DN	10	176	216	248	278	295	229	215	10	264	70	166	279
Patch size = 256 x 256 pixels (~13000 patches per camera per pipeline)													
RT	15	10	10	11	11	11	10	10	10	11	11	11	12
AT	10	54	52	47	52	53	44	58	10	62	15	27	41
LZ	11	111	153	132	154	158	131	135	10	151	36	83	114
DR	11	90	114	161	172	178	109	106	10	121	37	94	129
LR	11	103	132	174	201	207	128	124	10	141	44	111	150
AF	11	105	137	180	205	218	135	127	10	148	48	118	156
LM	11	126	174	173	203	209	309	183	10	232	58	138	160
DX	10	57	63	56	64	65	65	72	10	85	15	34	50
CI	10	10	10	11	10	10	10	10	932	10	10	10	11
LT	10	64	73	67	77	79	83	82	10	178	18	43	61
IN	10	14	16	19	19	20	18	14	10	18	37	17	19
UN	11	58	77	108	117	123	97	71	10	86	41	110	103
DN	10	43	54	63	70	73	54	52	10	64	20	42	67
Patch size = 128 x 128 pixels (~55000 patches per camera per pipeline)													
RT	11	10	10	11	11	11	10	10	10	10	11	11	11
AT	10	17	15	14	15	15	14	17	10	17	11	13	14
LZ	11	28	40	30	35	35	31	34	10	37	14	21	26
DR	11	21	26	38	40	42	24	24	10	27	14	24	30
LR	11	24	31	42	48	50	28	29	10	32	15	28	35
AF	11	24	32	43	49	52	29	29	10	33	15	29	36
LM	11	31	41	36	42	43	75	45	10	57	16	29	32
DX	10	17	17	16	16	16	17	20	10	22	11	13	15
CI	10	10	10	10	10	10	10	10	240	10	10	10	11
LT	11	18	19	17	18	18	21	22	10	46	12	14	16
IN	10	11	11	12	12	12	11	11	10	11	14	12	12
UN	11	16	19	26	29	30	21	18	10	20	15	28	25
DN	10	14	15	18	19	19	15	15	10	16	12	14	18

TABLE IV

TPR AT 0.5 % FPR USING PRNU PIPE (LIBRAW AND AFFINITY) AND TEST IMAGES (OF ALL PIPELINES) FOR CROSS-PIPELINE EXPERIMENTS

Camera	Camera Processing Pipelines for Test Images												
	RT	AT	LZ	DR	LR	AF	LM	DX	CI	LT	IN	UN	DN
PRNU pipe = LibRaw													
Patch size = 256 x 256 pixels (~40,000 patches per camera per pipeline)													
N7k	0.25	0.88	0.91	0.93	0.95	0.94	0.92	0.90	0.07	0.94	0.69	0.85	0.88
N90	0.06	0.68	0.75	0.73	0.77	0.76	0.69	0.73	0.06	0.72	0.47	0.68	0.58
C4D	0.72	-	0.72	0.73	0.75	0.75	0.70	0.73	0.67	0.73	0.44	0.22	0.62
C5D	0.69	-	0.69	0.68	0.69	0.70	0.64	0.68	0.63	0.67	0.47	0.57	0.59
Patch size = 128 x 128 pixels (~155,000 patches per pipeline)													
N7k	0.23	0.59	0.66	0.69	0.74	0.75	0.64	0.63	0.06	0.68	0.44	0.61	0.65
N90	0.07	0.47	0.54	0.54	0.58	0.58	0.46	0.49	0.06	0.48	0.26	0.48	0.41
C4D	0.45	-	0.43	0.49	0.50	0.51	0.43	0.45	0.38	0.42	0.23	0.10	0.40
C5D	0.51	-	0.51	0.51	0.54	0.55	0.44	0.49	0.42	0.45	0.28	0.42	0.43
PRNU pipe = Affinity													
Patch size = 256 x 256 pixels (~40,000 patches per camera per pipeline)													
N7k	0.26	0.89	0.92	0.93	0.95	0.94	0.92	0.90	0.07	0.94	0.70	0.86	0.88
N90	0.07	0.70	0.76	0.74	0.78	0.78	0.70	0.73	0.06	0.73	0.48	0.68	0.59
C4D	0.73	-	0.72	0.74	0.76	0.76	0.71	0.74	0.68	0.73	0.45	0.24	0.64
C5D	0.68	-	0.68	0.68	0.69	0.70	0.64	0.68	0.63	0.66	0.46	0.57	0.59
Patch size = 128 x 128 pixels (~155,000 patches per pipeline)													
N7k	0.21	0.60	0.67	0.70	0.75	0.76	0.65	0.63	0.06	0.69	0.46	0.62	0.66
N90	0.07	0.49	0.55	0.55	0.58	0.59	0.48	0.51	0.06	0.50	0.28	0.50	0.43
C4D	0.46	-	0.45	0.50	0.52	0.53	0.45	0.47	0.40	0.44	0.23	0.11	0.42
C5D	0.49	-	0.49	0.50	0.52	0.54	0.42	0.47	0.40	0.43	0.25	0.41	0.43

ing the most conservative setting with limited enhancement (e.g., default settings in darkroom software) and fixed selection

of images for PRNU estimation, we observed significant deterioration in all metrics, starting with fingerprint correlation, up to detection statistics and real-world performance metrics. This means that forensic analysts should be aware of a potential ISP mismatch, especially when using small analysis windows (e.g., manipulation localization) or when stronger enhancement or post-processing may be involved.

We experimented with 13 different pipelines representing various digital darkrooms and neural networks. The degradation was the strongest for smaller patches which are commonly used in photo manipulation detection. Specifically, for false positive rate fixed at 0.5%, an average deterioration of 17 percentage points was observed for patches of size 128 px (sample size 55,000) and 256 px (sample size 13,000). To illustrate qualitative impact on tampering localization, we show an example forgery and the corresponding authentication results in Figure 4. The depicted example is a synthetic forgery created by pasting a foreign patch of 1024 px inside a full resolution image taken with Nikon 7000 and processed by each pipeline. We show both local PCE responses and tampering probabilities obtained from  $p$ -values of PCE statistics [50]. It can be clearly observed that even for conventional darkroom software, the results exhibit strong variation.

We expect that the diversity of RAW processing pipelines, and increasing adoption of computational photography and machine learning (also directly inside of the cameras) will have more significant impact on PRNU analysis in the future. Negative impact of this variation is likely to be most pronounced not only in tampering localization, but also in reduced forms of PRNU used in large-scale search and attribution [27–30]. We have run exhaustive experiments, but in a limited, well-controlled lab setting. In most recent evaluations, other researchers are also starting to question fingerprint uniqueness in modern smartphones with advanced cameras [51]. Further work will be needed to assess the scope of the problem and to design new solutions. Some early work in this direction includes PRNU analysis in high-dynamic-range (HDR) photographs [52].

## ACKNOWLEDGEMENT

This material is based upon work partially supported by the overseas research experience fellowship, Indian Institute of Technology Gandhinagar (IITGN), the Department of Science and Technology (DST), Government of India under the Award Number ECR/2015/000583, and supported by Visvesvaraya Ph.D. Scheme, Ministry of the Electronics and Information Technology (MeitY), Government of India MEITY-PHD-951. Any opinions, findings, and conclusions or recommendations expressed in this material are those of the author(s) and do not necessarily reflect the views of the funding agencies.

## REFERENCES

- [1] M. A. Arbib, *Digital Image Forensics: There is More to a Picture than Meets the Eye*. USA, NY, New York: Springer, 2013.
- [2] A. Piva, "An overview on image forensics," *ISRN Signal Processing*, vol. 2013, pp. 1–22, Oct. 2012.
- [3] P. Korus, "Digital image integrity—a survey of protection and verification techniques," *Digital Signal Processing*, vol. 71, pp. 1–26, 2017.

- [4] J. Lukas, J. Fridrich, and M. Goljan, "Digital camera identification from sensor pattern noise," *IEEE Transactions on Information Forensics and Security*, vol. 1, no. 2, pp. 205–214, 2006.
- [5] X. Kang, J. Chen, K. Lin, and P. Anjie, "A context-adaptive spn predictor for trustworthy source camera identification," *EURASIP Journal on Image and Video Processing*, vol. 2014, no. 1, p. 19, 2014.
- [6] L.-B. Zhang, F. Peng, and M. Long, "Identifying source camera using guided image estimation and block weighted average," *Journal of Visual Communication and Image Representation*, vol. 48, pp. 471–479, 2017.
- [7] M. Al-Ani and F. Khelifi, "On the spn estimation in image forensics: A systematic empirical evaluation," *IEEE Transactions on Information Forensics and Security*, vol. 12, no. 5, pp. 1067–1081, 2017.
- [8] M. Chen, J. Fridrich, M. Goljan, and J. Lukás, "Determining image origin and integrity using sensor noise," *IEEE Transactions on Information Forensics and Security*, vol. 3, no. 1, pp. 74–90, 2008.
- [9] E. Quring and M. Kirchner, "Fragile sensor fingerprint camera identification," in *2015 IEEE International Workshop on Information Forensics and Security (WIFS)*. IEEE, 2015, pp. 1–6.
- [10] E. Quring, M. Kirchner, and K. Rieck, "On the security and applicability of fragile camera fingerprints," in *European Symposium on Research in Computer Security*. Springer, 2019, pp. 450–470.
- [11] A. Cortiana, V. Conotter, G. Boato, and F. G. De Natale, "Performance comparison of denoising filters for source camera identification," in *Media Watermarking, Security, and Forensics III*, vol. 7880. International Society for Optics and Photonics, 2011, p. 788007.
- [12] G. Chierchia, S. Parrilli, G. Poggi, C. Sansone, and L. Verdoliva, "On the influence of denoising in prnu based forgery detection," in *Proceedings of the 2nd ACM workshop on Multimedia in forensics, security and intelligence*, 2010, pp. 117–122.
- [13] M. Gharbi, G. Chaurasia, S. Paris, and F. Durand, "Deep joint demosaicking and denoising," *ACM Transactions on Graphics*, vol. 35, no. 6, pp. 1–12, nov 2016.
- [14] J. Lehtinen, J. Munkberg, J. Hasselgren, S. Laine, T. Karras, M. Aittala, and T. Aila, "Noise2noise: Learning image restoration without clean data," *arXiv preprint arXiv:1803.04189*, 2018.
- [15] G. Eilertsen, J. Kronander, G. Denes, R. Mantiuk, and J. Unger, "HDR image reconstruction from a single exposure using deep CNNs," *ACM Transactions on Graphics*, vol. 36, no. 6, pp. 1–15, nov 2017.
- [16] A. Ignatov, L. Van Gool, and R. Timofte, "Replacing mobile camera isp with a single deep learning model," *arXiv preprint arXiv:2002.05509*, 2020.
- [17] P. Korus and N. Memon, "Neural imaging pipelines—the scourge or hope of forensics?" *arXiv preprint arXiv:1902.10707*, 2019.
- [18] —, "Content authentication for neural imaging pipelines: End-to-end optimization of photo provenance in complex distribution channels," in *IEEE Conference on Computer Vision and Pattern Recognition*, 2019.
- [19] X. Kang, Y. Li, Z. Qu, and J. Huang, "Enhancing source camera identification performance with a camera reference phase sensor pattern noise," *IEEE Transactions on Information Forensics and Security*, vol. 7, no. 2, pp. 393–402, 2011.
- [20] X. Lin and C.-T. Li, "Enhancing sensor pattern noise via filtering distortion removal," *IEEE Signal Processing Letters*, vol. 23, no. 3, pp. 381–385, 2016.
- [21] C.-T. Li, "Source camera identification using enhanced sensor pattern noise," *IEEE Transactions on Information Forensics and Security*, vol. 5, no. 2, pp. 280–287, 2010.
- [22] M. Al-Ani, F. Khelifi, A. Lawgaly, and A. Bouridane, "A novel image filtering approach for sensor fingerprint estimation in source camera identification," in *2015 12th IEEE International Conference on Advanced Video and Signal Based Surveillance (AVSS)*. IEEE, 2015, pp. 1–5.
- [23] A. J. Cooper, "Improved photo response non-uniformity (prnu) based source camera identification," *Forensic science international*, vol. 226, no. 1-3, pp. 132–141, 2013.
- [24] H. Zeng and X. Kang, "Fast source camera identification using content adaptive guided image filter," *Journal of forensic sciences*, vol. 61, no. 2, pp. 520–526, 2016.
- [25] K. Dabov, A. Foi, V. Katkovnik, and K. Egiazarian, "Image denoising by sparse 3-d transform-domain collaborative filtering," *IEEE Transactions on image processing*, vol. 16, no. 8, pp. 2080–2095, 2007.
- [26] M. Kirchner and C. Johnson, "Spn-cnn: Boosting sensor-based source camera attribution with deep learning," *arXiv preprint arXiv:2002.02927*, 2020.
- [27] S. Bayram, H. T. Sencar, and N. Memon, "Sensor fingerprint identification through composite fingerprints and group testing," *IEEE Transactions on information forensics and security*, vol. 10, no. 3, pp. 597–612, 2014.
- [28] D. Valsesia, G. Coluccia, T. Bianchi, and E. Magli, "Compressed fingerprint matching and camera identification via random projections," *IEEE Transactions on Information Forensics and Security*, vol. 10, no. 7, pp. 1472–1485, 2015.
- [29] L. Bondi, P. Bestagini, F. Perez-Gonzalez, and S. Tubaro, "Improving prnu compression through preprocessing, quantization, and coding," *IEEE Transactions on Information Forensics and Security*, vol. 14, no. 3, pp. 608–620, 2018.
- [30] S. Taspinar, H. T. Sencar, S. Bayram, and N. Memon, "Fast camera fingerprint matching in very large databases," in *2017 IEEE International Conference on Image Processing (ICIP)*. IEEE, 2017, pp. 4088–4092.
- [31] A. G. Poyraz, A. E. Dirik, A. Karaküçük, and N. Memon, "Fusion of camera model and source device specific forensic methods for improved tamper detection," *arXiv preprint arXiv:2002.10123*, 2020.
- [32] C.-T. Li and Y. Li, "Color-decoupled photo response non-uniformity for digital image forensics," *IEEE Transactions on Circuits and Systems for Video Technology*, vol. 22, no. 2, pp. 260–271, 2011.
- [33] A. Mehrish, A. V. Subramanyam, and S. Emmanuel, "Sensor pattern noise estimation using probabilistically estimated raw values," *IEEE Signal Processing Letters*, vol. 23, no. 5, pp. 693–697, 2016.
- [34] —, "Robust prnu estimation from probabilistic raw measurements," *Signal Processing: Image Communication*, vol. 66, pp. 30–41, 2018.
- [35] D.-T. Dang-Nguyen, C. Pasquini, V. Conotter, and G. Boato, "Raise: A raw images dataset for digital image forensics," in *Proceedings of the 6th ACM Multimedia Systems Conference*. ACM, 2015, pp. 219–224.
- [36] V. Bychkovsky, S. Paris, E. Chan, and F. Durand, "Learning photographic global tonal adjustment with a database of input/output image pairs," in *CVPR 2011*. IEEE, 2011, pp. 97–104.
- [37] Rawtherapee. Accessed: May, 2019. [Online]. Available: <https://rawtherapee.com>
- [38] Aftershot pro 3 raw photo editor. Accessed: May, 2019. [Online]. Available: <https://www.aftershotpro.com/en/>
- [39] Lightzone. Accessed: May, 2019. [Online]. Available: <https://lightzoneproject.org/>
- [40] Dcraw: Decoding raw digital photos in linux. Accessed: May, 2019. [Online]. Available: <https://www.dechifro.org/dcraw/>
- [41] Libraw. Accessed: May, 2019. [Online]. Available: <https://www.libraw.org/>
- [42] Affinity photo. Accessed: May, 2019. [Online]. Available: <https://affinity.serif.com/en-us/>
- [43] Skylum luminar. Accessed: May, 2019. [Online]. Available: <https://skylum.com/luminar>
- [44] Dxomark. Accessed: May, 2019. [Online]. Available: <https://www.dxomark.com/>
- [45] Capture one. Accessed: May, 2019. [Online]. Available: <https://www.captureone.com/en/>
- [46] Lightroom. Accessed: May, 2019. [Online]. Available: <https://lightroom.adobe.com/>
- [47] M. Gharbi, G. Chaurasia, S. Paris, and F. Durand, "Deep joint demosaicking and denoising," *ACM Transactions on Graphics (TOG)*, vol. 35, no. 6, p. 191, 2016.
- [48] O. Ronneberger, P. Fischer, and T. Brox, "U-net: Convolutional networks for biomedical image segmentation," in *International Conference on Medical image computing and computer-assisted intervention*. Springer, 2015, pp. 234–241.
- [49] dcraw. Accessed: Jan., 2020. [Online]. Available: <https://en.wikipedia.org/wiki/Dcraw>
- [50] M. Goljan, "Digital camera identification from images—estimating false acceptance probability," in *International workshop on digital watermarking*. Springer, 2008, pp. 454–468.
- [51] M. Iuliani, M. Fontani, and A. Piva, "A leak in prnu based source identification? questioning fingerprint uniqueness," *arXiv preprint arXiv:2009.04878*, 2020.
- [52] D. Morshedi, M. Hosseini, and M. Goljan, "Camera identification from hdr images," in *Proceedings of the ACM Workshop on Information Hiding and Multimedia Security*, 2019, pp. 69–76.

TABLE V  
 MEDIAN PCE VALUES FOR CROSS-PIPELINE ATTRIBUTION OF NON-OVERLAPPING PATCHES FROM CANON EOS 40D

PRNU ISP	Image Processing Pipelines for Test Images												
	RT	AT	LZ	DR	LR	AF	LM	DX	C1	LT	IN	UN	DN
Patch size = 1024 x 1024 pixels (~600 patches per camera per pipeline)													
<b>RT</b>	<b>966</b>	-	758	888	1056	1163	1122	966	786	825	146	26	702
<b>AT</b>	-	-	-	-	-	-	-	-	-	-	-	-	-
<b>LZ</b>	869	-	<b>825</b>	949	1124	1094	1018	912	719	828	161	26	871
<b>DR</b>	688	-	610	<b>763</b>	873	957	840	696	607	641	106	24	607
<b>LR</b>	960	-	856	1168	<b>1319</b>	1359	1202	972	847	891	172	28	933
<b>AF</b>	1044	-	866	1122	1330	<b>1508</b>	1274	1072	876	966	158	31	939
<b>LM</b>	1166	-	948	1257	1476	1518	<b>1798</b>	1120	1086	1064	125	35	1007
<b>DX</b>	904	-	783	958	1066	1094	1046	<b>1048</b>	767	854	164	26	853
<b>C1</b>	460	-	366	493	570	575	650	473	<b>18923</b>	370	66	21	403
<b>LT</b>	849	-	777	953	1093	1085	1086	938	722	<b>3095</b>	145	26	817
<b>IN</b>	137	-	126	144	157	164	109	156	102	126	<b>1301</b>	19	136
<b>UN</b>	20	-	19	29	29	26	27	19	20	20	17	<b>75</b>	29
<b>DN</b>	715	-	633	853	940	1013	874	712	590	681	137	25	<b>964</b>
Patch size = 512 x 512 pixels (~3,000 patches per camera per pipeline)													
<b>RT</b>	<b>188</b>	-	163	179	201	213	206	193	164	178	32	14	120
<b>AT</b>	-	-	-	-	-	-	-	-	-	-	-	-	-
<b>LZ</b>	175	-	<b>186</b>	177	199	207	190	198	149	192	33	14	128
<b>DR</b>	134	-	124	<b>146</b>	166	176	145	137	115	131	25	14	103
<b>LR</b>	175	-	168	192	<b>214</b>	225	196	186	153	180	31	14	135
<b>AF</b>	201	-	188	229	254	<b>269</b>	230	207	177	201	33	15	156
<b>LM</b>	223	-	203	221	244	268	<b>332</b>	239	236	240	25	15	153
<b>DX</b>	177	-	178	166	188	202	198	<b>225</b>	165	199	35	14	121
<b>C1</b>	93	-	85	91	99	107	123	106	<b>5462</b>	98	18	13	66
<b>LT</b>	170	-	176	169	191	202	206	208	163	<b>723</b>	30	14	126
<b>IN</b>	26	-	27	29	29	29	19	32	21	27	<b>192</b>	13	28
<b>UN</b>	11	-	11	14	13	13	12	12	11	11	12	<b>22</b>	15
<b>DN</b>	124	-	119	136	151	162	141	137	106	131	27	14	<b>138</b>
Patch size = 256 x 256 pixels (~13,000 patches per camera per pipeline)													
<b>RT</b>	<b>48</b>	-	42	41	46	47	48	48	38	44	14	12	28
<b>AT</b>	-	-	-	-	-	-	-	-	-	-	-	-	-
<b>LZ</b>	47	-	<b>48</b>	42	46	47	46	50	37	48	15	12	30
<b>DR</b>	33	-	31	<b>37</b>	41	42	33	33	26	32	13	12	26
<b>LR</b>	44	-	41	48	<b>52</b>	54	43	44	35	43	15	12	34
<b>AF</b>	49	-	45	54	59	<b>62</b>	50	49	39	48	15	12	37
<b>LM</b>	56	-	52	49	55	56	<b>81</b>	60	58	61	13	12	35
<b>DX</b>	47	-	44	39	44	45	49	<b>58</b>	41	50	15	12	28
<b>C1</b>	25	-	22	23	24	24	31	28	<b>1517</b>	26	12	11	19
<b>LT</b>	45	-	44	39	43	44	51	53	40	<b>195</b>	14	12	28
<b>IN</b>	13	-	13	15	14	14	12	15	12	13	<b>48</b>	11	14
<b>UN</b>	10	-	10	12	11	11	11	11	10	10	11	<b>14</b>	12
<b>DN</b>	32	-	30	35	37	39	32	33	25	32	14	12	<b>33</b>
Patch size = 128 x 128 pixels (~55,000 patches per camera per pipeline)													
<b>RT</b>	<b>12</b>	-	12	12	11	12	11	12	11	11	10	11	12
<b>AT</b>	-	-	-	-	-	-	-	-	-	-	-	-	-
<b>LZ</b>	17	-	<b>21</b>	16	16	16	14	17	14	15	12	13	14
<b>DR</b>	13	-	14	<b>16</b>	15	15	12	14	12	13	11	13	14
<b>LR</b>	16	-	16	19	<b>20</b>	20	14	16	13	14	12	14	15
<b>AF</b>	15	-	16	18	18	<b>20</b>	13	15	13	14	12	14	15
<b>LM</b>	11	-	11	12	11	11	<b>12</b>	12	12	12	10	11	12
<b>DX</b>	15	-	16	15	14	15	17	<b>25</b>	16	17	12	12	13
<b>C1</b>	10	-	11	11	11	11	11	11	<b>397</b>	11	10	10	11
<b>LT</b>	11	-	12	12	11	12	12	13	11	<b>24</b>	10	11	11
<b>IN</b>	10	-	10	11	10	11	10	11	10	10	<b>12</b>	10	11
<b>UN</b>	13	-	13	14	14	14	12	12	12	12	11	<b>15</b>	13
<b>DN</b>	11	-	11	12	11	12	11	11	11	11	10	11	<b>12</b>

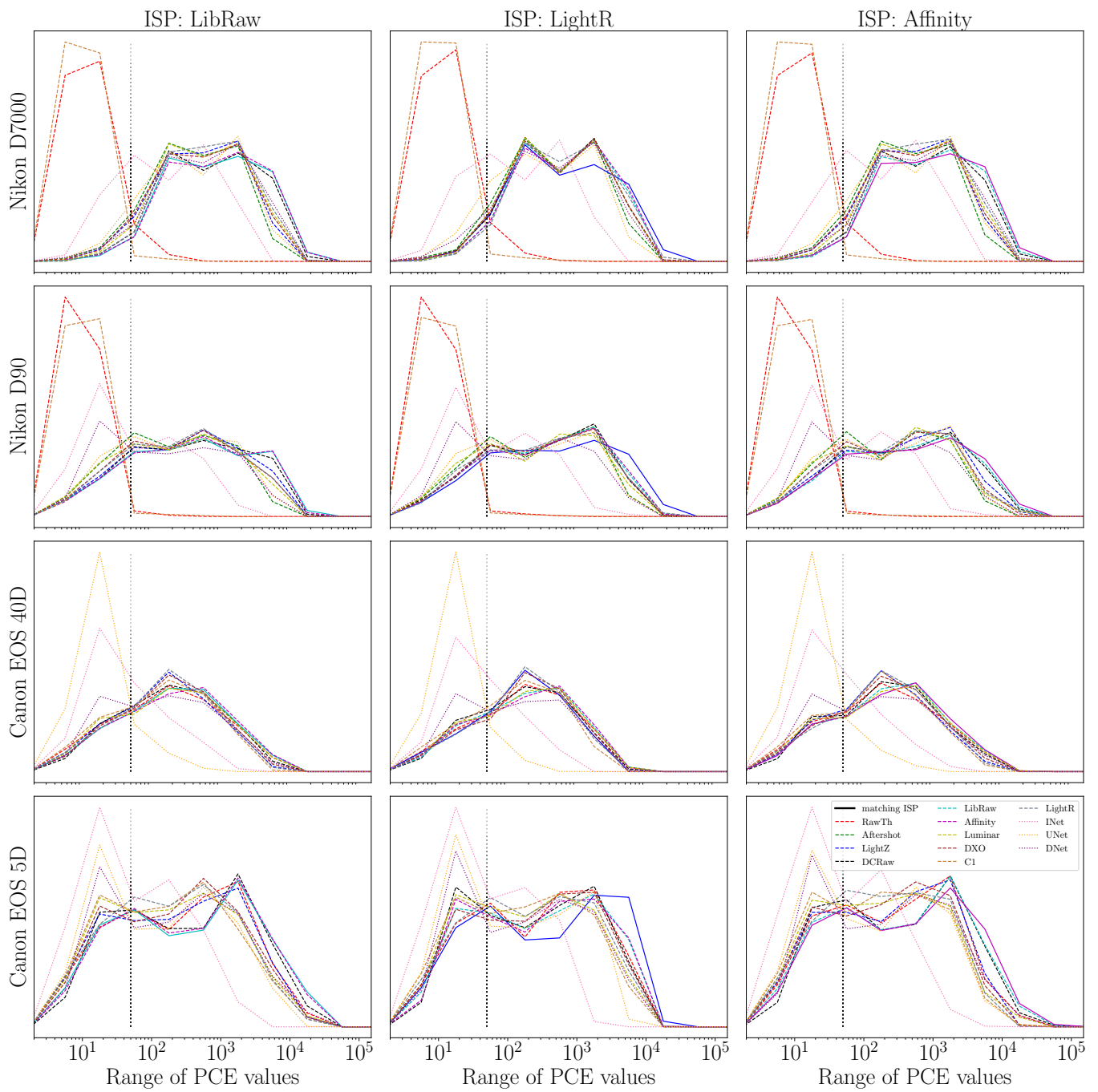


Fig. 5. Distribution of PCE scores for cross-ISP matching (512 px patches); the dashed vertical line shows a common acceptance threshold of 50.

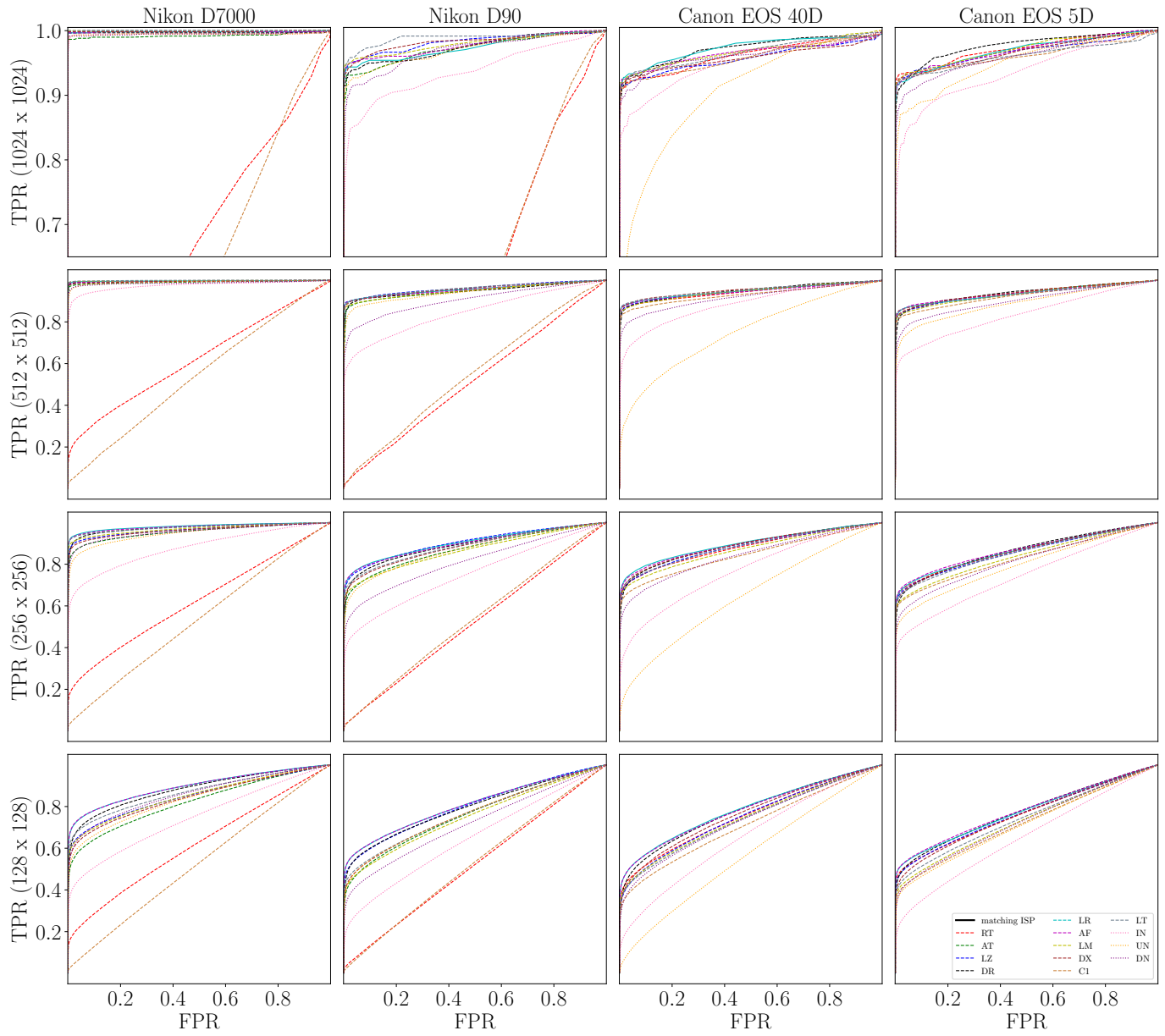


Fig. 6. Receiver operating characteristic (ROC) curves with LibRaw as PRNU estimation ISP and all pipelines as test.